Electrochimica Acta 213 (2016) 324–331

Contents lists available at ScienceDirect

Electrochimica Acta

journal homepage: www.elsevier.com/locate/electacta

Three-dimensional Inkjet Printed Solid Oxide Electrochemical Reactors. I. Yttria-stabilized Zirconia Electrolyte

N.M. Farandos, L. Kleiminger, T. Li, A. Hankin, G.H. Kelsall*

Department of Chemical Engineering, Imperial College London, London SW7 2AZ, UK

ARTICLE INFO

Article history:
Received 3 February 2016
Received in revised form 9 June 2016
Accepted 18 July 2016
Available online 22 July 2016

Keywords:
3D inkjet printing
yttria-stabilized zirconia (YSZ)
solid oxide electrochemical cell
CO_2 electrolysis

ABSTRACT

Solid oxide fuel cell (SOFC) and electrolyser (SOE) performances can be enhanced significantly by increasing the densities of (electrode | electrolyte | pore) triple phase boundaries and improving geometric reproducibility and control over composite electrode | electrolyte microstructures, thereby also aiding predictive performance modelling. We developed stable aqueous colloidal dispersions of yttria-stabilized zirconia (YSZ), a common SOFC electrolyte material, and used them to fabricate 2D planar and highly-customisable 3D microstructures by inkjet printing. The effects of solids fraction, particle size, and binder concentration on structures were investigated, and crack-free, non-porous electrolyte planes were obtained by tailoring particle size and minimising binder concentration. Micro-pillar arrays and square lattices were printed with the optimised ink composition, and a minimum feature size of 35 μm was achieved in sintered structures, the smallest published to-date. YSZ particles were printed and sintered to a 23 μm thick planar electrolyte in a Ni-YSZ|YSZ|YSZ-LSM|LSM electrolyser for CO_2 splitting; a feed of 9:1 CO_2:CO mixture at 1.5 V and 809 °C produced a current density of −0.78 A cm^{-2} even without more complex 3D electrode | electrolyte geometries.

1. Introduction

Diminishing fossil fuel reserves and concerns over CO_2-induced climate change and energy security have driven the rapid deployment of intermittent renewable energy conversion transducers, *e.g.* using solar and wind energy, to replace generation of electrical power using fossil fuels. To address their intermittency problem and to manage the dynamics of power demand, energy storage media for grid-scale applications should have high specific energy/energy densities, acceptable cost, and be abundant. One option is storing electrical energy in the bonds of carbon-based fuels such as CO and methanol, which can be derived from the electrolysis of CO_2, with round-trip energy conversion efficiencies of up to 72%, depending on current density, using a cyclically-operated solid oxide fuel cell (SOFC) and electrolyser (SOE) system [1]. Solid oxide electrochemical reactors are characterised by the use of a metal oxide as the electrolyte phase, *e.g.* yttria-stabilised zirconia $(ZrO_2)_{0.92}(Y_2O_3)_{0.08}$ (YSZ), and cermet electrodes based on *e.g.* nickel and lanthanum strontium manganite $La_{0.8}Sr_{0.2}MnO_{3-\delta}$ (LSM). The CO_2 electrolysis reactions occurring in each functional layer for both SOFC and SOE operation are:

Porous Ni-YSZ:

$$CO_2 + 2e^- \underset{SOFC}{\overset{SOE}{\rightleftarrows}} CO + O^{2-} \quad (1)$$

YSZ electrolyte:

$$O^{2-}(\text{cathode}) \underset{SOFC}{\overset{SOE}{\rightleftarrows}} O^{2-}(\text{anode}) \quad (2)$$

Porous LSM-YSZ:

$$\frac{1}{2}\left(2O^{2-} \underset{SOFC}{\overset{SOE}{\rightleftarrows}} O_2 + 4e^-\right) \quad (3)$$

Three types of processes have been reported for fabricating the functional layers of SOFC/SOEs: chemical methods, physical methods, and ceramic powder processes [2]. Conventional powder processing methods involve mixing the constituent phases in powder form with a sacrificial pore-forming phase to form pastes that are tape cast or screen printed into films, then subsequently dried and sintered. Such techniques result in poorly reproducible structures, porosities, and densities of so-called triple phase boundaries (TPBs) that are the intersections of individually

* Corresponding author. Tel.: +44 0 20 7594 5633.
E-mail address: g.kelsall@imperial.ac.uk (G.H. Kelsall).

http://dx.doi.org/10.1016/j.electacta.2016.07.103
0013-4686/

Table 1
Physical properties and composition of formulated inks (Inks 1–5).

Ink #	Viscosity/mPa s	Surface tension/mN m^{-1}	Oh^{-1}	YSZ fraction/wt%	PEG concentration/mg cm^{-3}	Particle size/nm	Particle specific surface area/m^2 g^{-1}	Droplet volume/pL	Ejection velocity/m s^{-1}	D_m/D_i
1	4.7[a)]	24	8.5	24	25	194	9.2	29	4.5	1.6
2	4.1[b)]	24	9.1	20	25	115	10.8	30	4.5	1.7
3	8.8[a)]	25	4.4	10	40	194	9.2	29	4.5	1.8
4	7.5[a)]	25	5.1	10	40	115	10.8	27	4.5	2.7
5	4.2[a)]	28	9.2	3	30	194	9.2	20	2.8	2.8

[a)]Newtonian viscosities; [b)]Shear shinning behaviour observed; viscosity of 4.1 mPa s was that at an infinite shear rate. See Supporting Information Table S1.
D_m/D_i corresponds to the individual droplet resolution, *i.e.* ratio of the maximum spread diameter of a droplet on a substrate (D_m), the so-called splat diameter, to the in-flight diameter (D_i).

percolated pores, electronically-conducting and ionically-conducting phases, at which reactions occur [3]. Hence, microstructural engineering is critically important in improving electrochemical performance [4]. Infiltrated-scaffold techniques with higher TPB densities and control over porosity are being developed [5,6], the scaffolds being fabricated by tailored sintering of a ceramic film mixed with a pore-forming phase [7], or by mining 'trenches' in pre-densified ceramic films with an excimer laser [8].

Additive manufacturing techniques offer the potential to fabricate the functional layers of SOFCs and SOEs with high reproducibility and level of customization. Inkjet printing is particularly suited to fabrication of thin films from precursor colloidal particle dispersions ('inks'), [9], and has been deployed to produce layers of YSZ [10–14], gadolinium-doped ceria (CGO) [15–18], LSM [15], and lanthanum strontium cobalt ferrite (LSCF) [17,19,20], but never to produce 3D scaffolds. Inks typically employ organic solvents (*i.e.* α-terpineol or alcohols) in which to disperse particles due to their relatively high viscosity and low surface tension, ensuring stability and printability. However, aqueous dispersions are preferable environmentally and for large scale industrial deployment.

One prerequisite to inkjet printing is the development of stable dispersions ('inks') of sub-micrometre sized metal oxide particles (*i.e.* YSZ, NiO, LSM etc.) in liquid phases with suitable solids fractions and physical properties, to enable printing of the functional layers of SOFCs/SOEs. These requirements are encompassed by the dimensionless Ohnesorge (Oh) number, which is the ratio $We^{0.5}/Re$, defined in Eqs. (4)–(6), *i.e.* the ratio of viscous forces to inertia and surface tension forces.

$$We = \frac{\rho u^2 r}{\gamma} \tag{4}$$

$$Re = \frac{\rho u r}{\eta} \tag{5}$$

$$Oh = \frac{\eta}{\sqrt{\rho \gamma r}} \tag{6}$$

Where We is the Weber number, Re the Reynolds number, and ρ, η, γ represent the ink density, viscosity, and surface tension, respectively, u is the ejection velocity, and r is the characteristic length, typically the diameter of the printhead nozzle [21]. The range of permissible physical properties is constrained by printability, *i.e.* stable and consistent droplet ejection [22], as suggested in Eq. (7), and to ensure droplet ejection [23], by condition (8).

$$1 < Oh^{-1} < 10 \tag{7}$$

$$We > 1 \tag{8}$$

Herein, we report firstly a technique for formulating aqueous dispersions of YSZ particles, stable to aggregation over weeks, and that were employed subsequently as inks to print reproducible planar and 3D microstructures for SOFCs and SOEs. The suitability of printed structures for the electrolyte phase in SOFCs was assessed, varying ink formulation by changing particle size, solids fraction, polymer binder concentration and viscosity. Secondly, we report results for splitting CO_2 over a range of temperatures in a Ni-YSZ|YSZ|LSM-YSZ|LSM reactor with a planar printed electrolyte, the first results for a SOE fabricated by inkjet printing published to-date. Subsequent publications will address effects of 3D printed electrode | electrolyte structures on SOE/SOFC performances.

2. Experimental

2.1. Ink Formulation

Dispex A40 (Ciba-BASF, UK) was dissolved in de-ionized water at a concentration of 0.2 mg m^{-2} of 8 mol% yttria-stabilized zirconia (YSZ) particles. Two sizes of YSZ particles were investigated, the larger from Sigma Aldrich, USA, and the smaller from Fuel Cell Materials, USA. The particles were then added and dispersed by direct exposure to an ultrasonic probe (Q55, 20 kHz, 6 mm Ti alloy tip, QSonica, USA) with three 3 minute bursts at 60% amplitude, and 3 minute cooling intervals between each. The resulting dispersions were stirred for 24 h, centrifuged (Eppendorf Centrifuge 5810 R, Germany) at relative centrifugal forces of 1350 for 2 minutes, and 1000 for 5 minutes, for the larger and smaller particles, respectively, to narrow particle size distributions, and then filtered to remove particles with a diameter exceeding 800 nm. Polyethylene glycol 35,000 (PEG 35000) (Sigma Aldrich, USA) was added to the filtrate and allowed to dissolve for 24 h. Immediately prior to printing, the alcohol ethoxylate Natsurf 265 (Croda Chemicals, UK) was added at a concentration of 0.2 mg cm^{-3} of the total volume of the ink. Compositions of formulated inks are given in Table 1.

2.2. Substrate Fabrication

Nanometre and micrometre NiO particles (NiO(nm) and NiO (μm), respectively) (Inframat Advanced Materials, USA) and nanometre YSZ particles (Inframat Advanced Materials, USA and Sigma Aldrich, USA, YSZ(I) and YSZ(S), respectively) were individually, and as 60:40 wt% mixtures, compressed into cylinders of *ca.* 3–4 mm height using a tablet press with a 1700 kg cm^{-2} load (Gamlen Tableting Ltd., UK). The shrinkage behaviour was analysed in a dilatometer (Netzsch model DIL 402C) in static air, heating the samples to 1500 °C at 5 °C min^{-1}, dwelling the samples for 10 hours, followed by cooling to room temperature.

A NiO-YSZ slurry was prepared by mixing the constituent powders at 60:40 wt% ratio of NiO(μm) and YSZ(I), respectively, with polyethersulfone (PESf) (Radel A-300, Ameco Performance, USA) as a binder and polyethyleneglycol 30-dipolyhydroxystearate (Arlacel P135, Uniqema, USA) dispersant in dimethyl sulfoxide (Sigma Aldrich, USA), using a planetary miller at mass ratios 200:25:2:100 (NiO-YSZ, binder, dispersant, solvent) respectively. The substrate was then fabricated via a phase inversion-assisted tape casting process with an adjustable casting knife gap. The resultant sheets were soaked in an external coagulant (water) bath for 24 h to allow the phase inversion to complete, and subsequently flattened and dried.

2.3. Printing 2D and 3D Structures

A CeraDrop X-Serie piezoelectric drop-on-demand inkjet printer (Ceradrop, Limoges, France) with a Dimatix Sapphire QS-256/30 AAA printhead (Fujifilm, Japan) was used to deposit the dispersions onto the NiO-YSZ substrate. The diameter of the printhead nozzles was 52 μm [24]. The drying time between each printed layer for 2D planar structures was 240 s at an ambient temperature of 26–28 °C. The droplet deposition pattern was a square lattice (*i.e.* a coordination number of 4 for each droplet) for all printed structures; however, droplet overlap (diameter overlap between coordinated pairs) varied between 20–40%.

To print 3D pillars, separate arrays of heights of 50 and 180 layers were printed directly onto the NiO-YSZ substrates, with 120 s drying times between each successive layer. The pillar geometries corresponded to a mixture of single droplets ('splats') and double splats overlapped at 67%. The square scaffold was printed directly onto the NiO-YSZ substrate with a droplet overlap of 50%.

2.4. Sintering

The printed structures were heated at a rate of 4 °C min^{-1} to 600 °C, at which they were held for 6 h under an air atmosphere (Elite Thermal Systems furnace, UK), then heated at a rate of 15 °C min^{-1} to 1500 °C, at which they were held for 10 h, before being cooled at 4 °C min^{-1} to room temperature.

2.5. Reactor Fabrication

Twelve layers of Ink 1 were deposited onto the substrate. The printer settings were an 80 V pulse applied to the piezoelectric nozzles with a total pulse duration of 13 μs, including an increase and decrease time of 2 and 5 μs, respectively, at a frequency of 2.8–5 kHz. The printed layer and substrate were co-sintered, as above. A LSM-YSZ paste (Fuel Cell Materials, USA) was brush-coated on the electrolyte and allowed to dry at room temperature, followed by a coating of LSM paste (Fuel Cell Materials, USA). After drying, the cells were sintered at 1100 °C for 3 h with a ramp rate of 4 °C min^{-1}.

2.6. Characterisation

2.6.1. Material and Ink Characterisation

Specific surface areas and porosities of yttria-stabilized zirconia powders were determined using a Micrometrics 3Flex machine (Canada), by applying Brunauer-Emmett-Teller (BET) theory, first degassing 300 mg samples of each powder at 200 °C, followed by N_2 adsorption. Particle sizes were determined after formulating inks by diluting the dispersions sufficiently to allow dynamic light scattering to be applied, using a Zetasizer μV instrument (Malvern, UK).

Viscosities of dispersions were measured with a DV-E viscometer (Brookfield, UK) after they had been stirred for 24 h; surface tensions were measured using a capillary tensiometer (Cole Parmer, USA).

2.6.2. Microstructural Characterisation

Scanning electron microscopy (SEM) was performed at 20 kV, 15 mm working distance with 10 mm chromium coating (JSM 6400, JEOL, USA) to image the complex structures. The cross-sections of the printed cells were imaged using a Hitachi TM3030 SEM at 15 kV accelerating voltage.

2.7. Electrochemical Behaviour

2.7.1. Current Collection, Sealing and Reactor Assembly

Current collection from the electrodes was via a silver mesh (80 mesh, woven from 0.115 mm diameter wire, Alfa Aesar, UK), silver paste (Alfa Aesar, UK) and silver wire (0.25 mm diameter, 99.9% purity, annealed, VWR International, UK). The cell was cemented to an alumina tube using a ceramic sealant (Aron Ceramic D, Aron Alpha Toagosei, USA). Gases were supplied and extracted via a stainless steel end-cap sealed with Viton O-rings (Polymax, UK) against the alumina tube. A schematic of the reactor is shown in Fig. 1.

2.7.2. Electrolyser Performance Experiments

The NiO was reduced to Ni at 670 °C in a 25–75 H_2-He gas atmosphere for 2 h after being heated at 4 °C min^{-1} in a pure He atmosphere (Elite Thermal Systems Ltd., UK). After reduction, the cell was heated progressively to the operating temperatures (718, 764 and 809 °C) monitored by a K-type thermocouple. The operational gas feed molar compositions were 9:1 CO_2:CO with

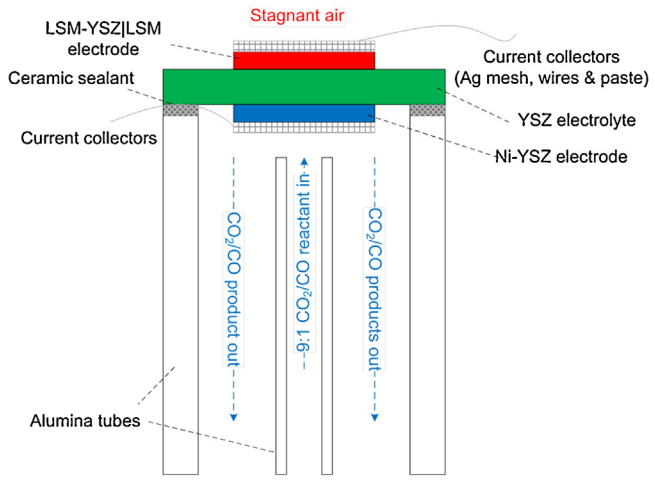

Fig. 1. Planar CO_2(-CO) | Ni-YSZ | YSZ | YSZ-LSM | LSM | O_2 cell experimental assembly.

40 ml min^{-1} total flow rate, controlled by an automated mass-flow controller (Bronkhorst, UK), as were all gas flow rates. The LSM-YSZ oxygen electrode (electrolyser anode) was operated in static air.

Four-probe measurements were made by connecting the silver wires to a potentiostat/galvanostat capable of electrochemical impedance measurements using a frequency analyser (FRA) 4.9 module with test procedures created in the Nova 1.10.2 software (PGSTAT302N, Metrohm Autolab B.V., Netherlands). The potential difference response of the cell to linearly scanned applied current was measured, as was the electrochemical impedance at open circuit potential difference (OCPD) with a RMS amplitude of 0.01 V over a frequency range 10^5-0.1 Hz.

The gaseous product composition from the Ni-YSZ cathode was measured using on-line mass spectrometry (Genesys 200D, ESS Ltd, UK) to determine the charge yield of the cell.

3. Results and Discussion

3.1. Printing 2D and 3D Structures

3.1.1. Ink Characterisation

Five different aqueous inks were formulated, varying the solids fraction, particle size distributions and PEG concentration to the compositions reported in Table 1, to investigate their effects on the fabricated structures. The physical properties of all formulations lay within the range of printability, *i.e.* $1 < Oh^{-1} < 10$ [22], where Oh represents the ratio of viscous forces to inertial and surface tension forces. Stability against aggregation was confirmed by the absence of sedimentation over a period of weeks.

Fig. 2 shows the particle size distributions of the formulated inks, particle size being an important parameter for inkjet printing of colloidally dispersed solids, as particles should be sufficiently small, *inter alia*, to avoid blocking the nozzles during printing.

3.1.2. Crack Mitigation within 2D Planar Structures

Thin, gas-tight, planar structures of each ink were printed to assess their ability to resist cracking, which would otherwise create gas leaks in the sintered electrolyte layer or mechanical failure in complex microstructures. In the green films, cracks form during drying in response to a capillary pressure gradient throughout the film, due to evaporation-driven flows that result from the relatively high surface tension of water [25]. Inks 1 and 5 resulted in planes that did not crack; however, Inks 2–4 cracked (Fig. 3), which can be explained as follows.

The critical cracking thickness (H_{crit}), the film depth below which cracking does not occur, depends on the shear modulus of the YSZ particles (G), the particle packing density (ϕ), coordination number (N), particle radius (R), Poisson ratio (ν), and the surface tension of the ink (γ), according to equation (9) [26].

$$\frac{H_{crit}}{R} = 0.050\left(\frac{GN\phi R}{2\pi(1-\nu)\gamma}\right)^{2/3} \quad (9)$$

It is essential that the thickness of a single dried printed layer (H) is lower than H_{crit}, as when printing isolated droplets (*i.e.* narrow structures in the x-y plane), the rate of evaporation (E) is high, so the ability to mitigate cracking is determined by the condition: $H < H_{crit}$. At low E, cracking may be avoided at $H > H_{crit}$. Assuming that the particles were spherical and assembled in a random close packing (RCP) arrangement in the printed film (*i.e.* $N = 6$, $\phi = 0.6$), this would indicate that the critical cracking thickness for Inks 1–5 was 18, 7, 17, 7, and 16 μm, respectively, using models to predict G and ν [27]. In reality, H_{crit} would be expected to differ from these values for some formulations for three reasons:

1) Particles were non-spherical and their average size did not represent all particles in the distribution.
2) Strong inter-particle interactions may cause aggregation, decreasing the particle packing fraction.
3) For printed layer number n, where $n > 1$, the 'substrate' is a previously printed layer, and consequently it may be possible for cracks to enter the substrate, decreasing the structure's potential to withstand cracking, *i.e.* $H_{crit}(n > 1) < H_{crit}(n = 1)$ [28].

However, it was also evident that packing arrangement ($N.\phi$) varied with organic additive composition, as cracking behaviour was inconsistent for constant R. This can be explained by considering the processes that occur during droplet drying. As the water evaporates, the particles (and polymer) are concentrated within the printed film. If the particles are brought sufficiently close together, they may overcome electrostatic repulsion and aggregate. In addition, if there is a free polymer present in the drying droplet, a depletion potential may be induced if its concentration is sufficiently high, and inter-particle separation sufficiently low (*i.e.* excluded volumes). The packing density within these aggregates ultimately determines the packing density within the printed films, if the inter-particle potentials are greater than the capillary pressure. As polymer concentration is increased further during drying, a stabilization potential is induced, locking the particles in their existing arrangement, as shown in Fig. 4.

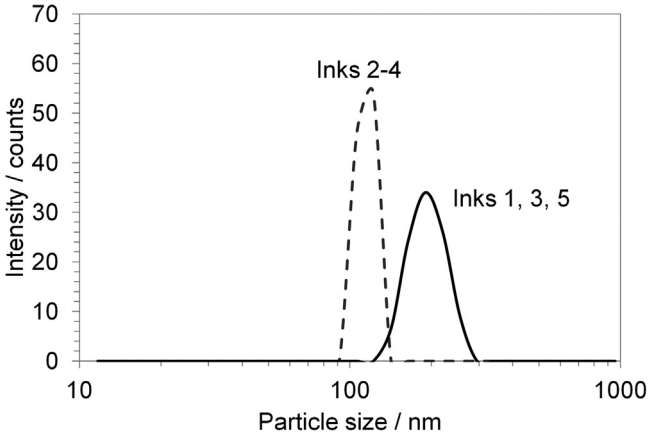

Fig. 2. Particle size distributions for Inks 1–5.

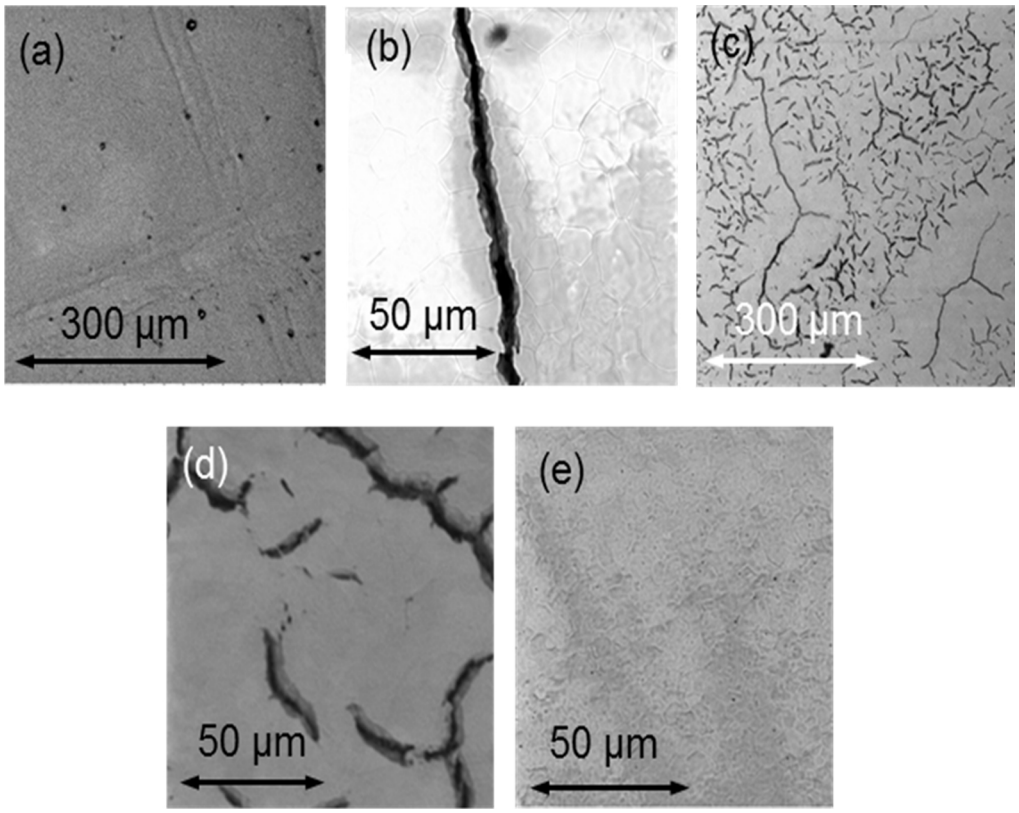

Fig. 3. SEM surface view images of sintered planar structures fabricated with (a) 12 layers of Ink 1, (b) 25 layers of Ink 2, (c) 16 layers of Ink 3, (d) 40 layers of Ink 4, and (e) 20 layers of Ink 5. Droplet overlap was 40% for Ink 1, and 20% for Inks 2–5.

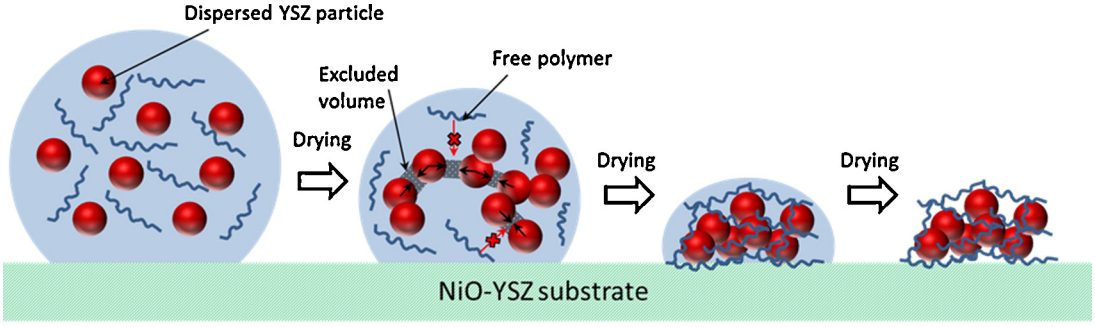

Fig. 4. Schematic of the depletion potential induced by free polymer due to the excluded volume between particles, inducing a stabilization potential as drying progresses.

Inks 1 and 2 both had a concentration of 25 mg cm^{-3} PEG and similar surface coverage per printed layer (3.4 and 2.2 monolayers equivalent, respectively); however, Ink 2 cracked and Ink 1 did not. This can be attributed to the smaller YSZ particle size of Ink 2, which decreased the critical cracking thickness (H_{crit}) by 60%. In addition, as the droplet overlap for Ink 1 was 40%, rather than 20% for Ink 2, the volume of deposited ink was approximately 90% greater in the former case for a given printed area, so the surface area to volume ratio was approximately 50% lower than for the case of Ink 2, which decreased E, so even $H > H_{crit}$ could be tolerated. However, the condition $H > H_{crit}$ was unlikely for Ink 1 as 'green' printed pillars of *ca.* 60 μm diameter, *i.e.* a single splat, did not crack. The packing density of particles in Ink 1 was 64%, corresponding to random close packing, so it can be inferred that the rate and extent of particle aggregation during drying was insufficient to decrease the packing density.

Inks 3 and 4 had an increased free polymer concentration of 40 mg cm^{-3} and decreased surface coverage per printed layer (0.4–0.5 monolayer equivalent). They also had lower YSZ particle fractions, which would suggest they were more stable dispersions than Inks 1 and 2, so would form denser aggregates; however, this was not the case, as cracking was observed for both inks. Therefore, it is proposed that the increase in concentration of the polymer during drying contributed to an increased (attractive) depletion potential between the particles, inducing aggregation, and that this progressed sufficiently to decrease $N.\phi$ (*i.e.* $(N.\phi) < 6 \times 0.64$). When the stabilization potential was induced as drying progressed, the aggregates became locked in a kinetically immobile state, so the overall packing density was lower than for Inks 1 and 2. This state could resist deformation due to residual capillary pressures, so the particles did not rearrange into a closer-packed state. Notably, the depletion potential was greater for the larger YSZ particles (Ink 3),

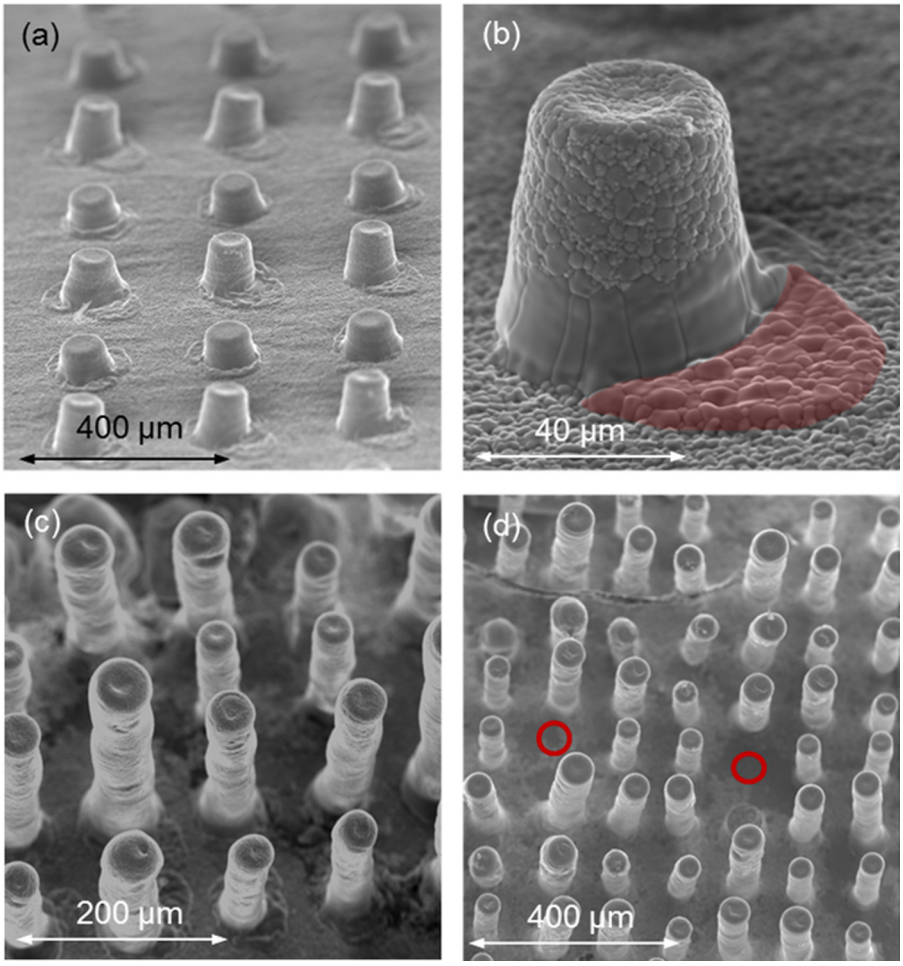

Fig. 5. SEM images of YSZ pillars on Ni-YSZ substrate. (a) Array of 50 layer pillars at 60° tilt; (b) showing the remnants of a misplaced droplet (red zone) and 50 layer pillar, (c) pillar array 180 layers tall (ca. 300 μm) at 30° tilt, and (d) pillar array showing missing pillars (red circles) due to inactive nozzles (For interpretation of the references to colour in this figure legend, the reader is referred to the web version of this article.).

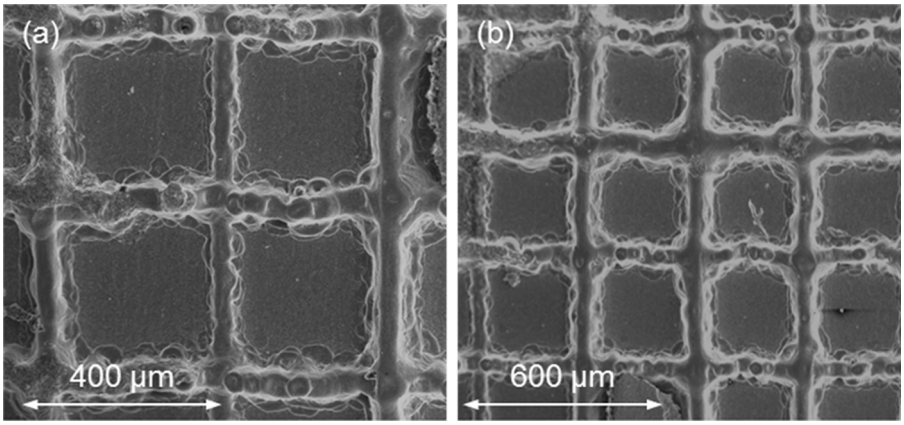

Fig. 6. SEM images of YSZ square scaffolds.

as the particle-particle excluded volume is proportional to R^6, so the factor $N.\phi$ was lower for Ink 3 than Ink 4. The absolute value of $N.\phi$ is difficult to predict due to the combination of aggregation kinetics and evaporation-driven flows.

Alternatively, cracking in Inks 3 and 4 could have been due to the lower surface coverage than for Inks 1 and 2 as >5 times as many layers were required to form a film of equivalent thickness. Hence, particles that were deposited in subsequently printed layers interacted with particles that had been deposited in previously printed layers to form aggregates with low packing densities. However, this can be excluded as the surface coverage for Ink 5 was 5% monolayer equivalent, *i.e.* 65 times the number of layers were required to fabricate a structure of equivalent thickness to Ink 1 and cracking was not observed. As the deposited solid was 5% monolayer equivalent for Ink 5, particle separation upon deposition was sufficiently large to neglect depletion

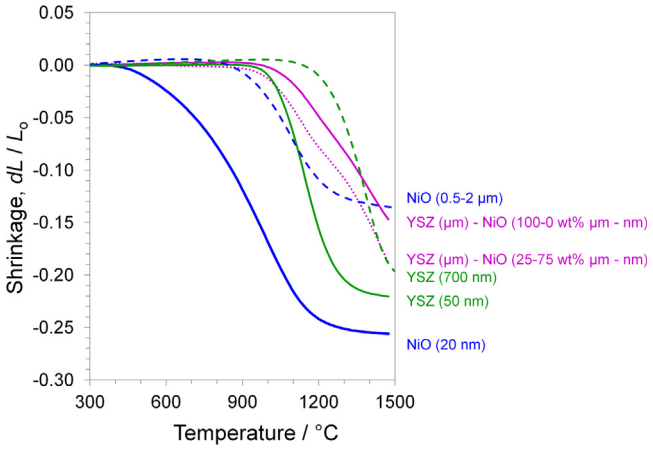

Fig. 7. Sintering behaviour of nano- and micrometre NiO, YSZ and NiO-YSZ mixtures with varying nano- and micrometre particle contributions to the NiO-YSZ component.

potentials, so a random close packed structure resulted. This also meant that previously deposited polymer was not re-dispersed by subsequently (wet) printed layers, so it is also unlikely that cracks can enter the NiO-YSZ substrate.

3.2. Printing 3-D Microstructures

Although Ink 5 formed a crack-free layer and was suited to printing ultra-thin films, Ink 1 was preferable, as solid deposition rates were much faster for building microstructures. As shown in Fig. 5, using Ink 1, the minimum feature resolution achieved in sintered structures in the x-y (horizontal) plane was 35 µm, and in the z-direction 1.2 µm, the smallest reported feature resolution to-date. The maximum height of structures was ca. 300 µm and the tops of the pillars were concave due to a mild 'coffee staining' effect [29].

In addition, square scaffolds with a minimum feature-resolution of 40 µm were printed, demonstrating the technique's high degree of customization (Fig. 6). The packing fraction of YSZ in the green printed structures was 0.64, corresponding to random close packing, resulting in highly dense sintered structures. Hence, these results demonstrate the potential of using inkjet printing to fabricate 3D scaffolds that can be infiltrated post-sintering for use in SOFCs and SOEs.

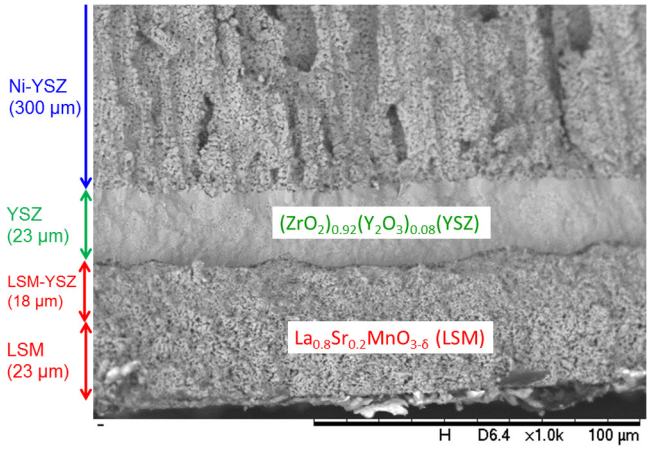

Fig. 8. SEM image of cross-section of Ni-YSZ|YSZ|YSZ-LSM|LSM cell post-operation, with thicknesses of each layer.

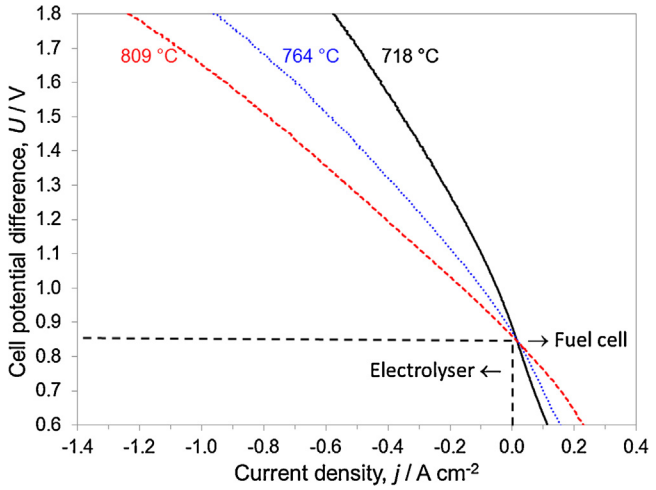

Fig. 9. Effects of temperature and applied current density on CO_2(-CO) | Ni-YSZ | YSZ | YSZ-LSM | LSM | air cell potential differences.

3.3. Electrolyser with Printed Electrolyte

3.3.1. Characterisation of the Substrate

Fig. 7 shows the shrinkage behaviour of the individual constituent powders and mixtures. NiO and YSZ are inherently mismatched in their sintering behaviour, but by combining nanometre- with micrometre-sized particles, essentially creating a bimodal particle size distribution, the final shrinkage of the NiO-YSZ substrate could be tailored to match that of a printed YSZ layer. This prevented stresses during sintering and enabled a flat, crack-free NiO-YSZ|YSZ dual-layer that could be co-sintered.

The printed YSZ electrolyte layer was dense, crack-free and adhered well to the Ni-YSZ substrate (Fig. 8), contrary to the low densities commonly reported as a limitation of inkjet printing. After sintering, the total thickness of the printed electrolyte layer was *ca.* 23 µm, corresponding to *ca.* 2 µm for each of the 12 printed layers; hence, there is scope for decreasing the electrolyte layer thickness, without compromising gas-tightness.

3.3.2. Electrochemical Performance

The open circuit potential differences were measured as 0.88 to 0.84 V at 718 °C and 809 °C, respectively, which were close to the theoretically calculated values [30]. Current densities achieved at the thermo-neutral potential difference (*ca.* 1.5 V) were between −0.35 and −0.78 A cm^{-2} (Fig. 9) in the temperature range investigated. Charge yields of unity were confirmed by mass spectrometric concentration measurements of CO_2 reduced and

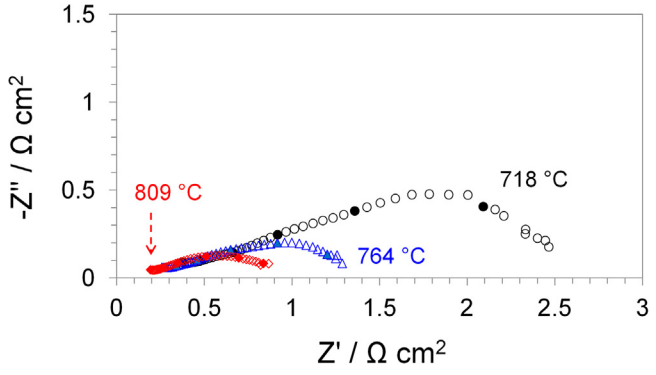

Fig. 10. Electrochemical impedance spectra of CO_2(-CO) | Ni-YSZ | YSZ | YSZ-LSM | LSM | air cell at 718, 764 and 809 °C; filled markers indicate frequency decades (10^5–0.1 Hz).

CO produced. The maximum CO_2 conversion achieved was *ca.* 20% resulting in a CO to CO_2 ratio of 3:7. Hence, coking was not expected to occur, as the CO equilibrium fraction for the Boudouard reaction is 0.7–0.91 [31].

The cell performance, as indicated by the area specific resistance, was dominated by the electrode polarisation contributions (Fig. 10), due mainly to the tape-casted Ni-YSZ substrate porosity not yet being optimised, so restricting gas diffusion limited current densities. Hence, in the future, the substrate will be printed and the electrolyte thickness decreased further, the limit being set by the 2 μm thickness per printed layer for the particular ink used.

4. Conclusions

Planar and 3D YSZ electrolyte structures were fabricated by inkjet printing requiring prior formulation of five aqueous inks with varying particle size and viscosity. It was found that tailoring particle size and polymer binder concentration enabled crack-free electrolyte planes to be printed and subsequently sintered. Micro-pillar arrays and square lattices were printed subsequently with the optimal ink formulation, resulting in crack-free 3D microstructures with a minimum feature resolution of 35 μm in the horizontal plane. The performance of a Ni-YSZ|YSZ|YSZ-LSM|LSM electrolyser for CO_2 splitting with a 23 μm thick inkjet-printed YSZ electrolyte was then determined using a CO_2/CO mixture with a molar ratio of 9:1; at 809 °C, a current density of $-0.78\ A\,cm^{-2}$ was achieved at 1.5 V, the thermo-neutral potential difference.

Supporting Information

Supporting Information is available from the Elsevier website.

Acknowledgements

The authors thank the UK EPSRC for post-doctoral research associateships for L.K. and T.L., and Imperial College London for a research studentship for N.M.F., who contributed equally with L.K.

References

[1] L. Kleiminger, T. Li, K. Li, G.H. Kelsall, CO_2 splitting into CO and O_2 in micro-tubular solid oxide electrolysers, RSC Advances 4 (2014) 50003–50016.
[2] J. Will, A. Mitterdorfer, C. Kleinlogel, D. Perednis, L.J. Gauckler, Fabrication of thin electrolytes for second-generation solid oxide fuel cells, Solid State Ionics 131 (2000) 79–96.
[3] P.S. Jørgensen, S.L. Ebbehøj, A. Hauch, Triple phase boundary specific pathway analysis for quantitative characterization of solid oxide cell electrode microstructure, J. Power Sources 279 (2015) 686–693.
[4] A. Atkinson, S. Barnett, R.J. Gorte, J.T.S. Irvine, A.J. McEvoy, M. Mogensen, S.C. Singhal, J. Vohs, Advanced anodes for high-temperature fuel cells, Nat Mater 3 (2004) 17–27.
[5] J.M. Vohs, R.J. Gorte, High-Performance SOFC Cathodes Prepared by Infiltration, Adv. Mater. 21 (2009) 943–956.
[6] E.D. Wachsman, K.T. Lee, Lowering the Temperature of Solid Oxide Fuel Cells, Science 334 (2011) 935–939.
[7] M. Kishimoto, M. Lomberg, E. Ruiz-Trejo, N.P. Brandon, Enhanced triple-phase boundary density in infiltrated electrodes for solid oxide fuel cells demonstrated by high-resolution tomography, J. Power Sources 266 (2014) 291–295.
[8] K. Nagato, S. Shinagawa, N. Shikazono, S. Iwasaki, M. Nakao, SOFC Anode Based on YSZ Pillars, ECS Transactions 68 (2015) 1309–1314.
[9] C. Li, H. Chen, H. Shi, M.O. Tade, Z. Shao, Green fabrication of composite cathode with attractive performance for solid oxide fuel cells through facile inkjet printing, J. Power Sources 273 (2015) 465–471.
[10] V. Esposito, C. Gadea, J. Hjelm, D. Marani, Q. Hu, K. Agersted, S. Ramousse, S.H. Jensen, Fabrication of thin yttria-stabilized-zirconia dense electrolyte layers by inkjet printing for high performing solid oxide fuel cells, J. Power Sources 273 (2015) 89–95.
[11] D. Young, A.M. Sukeshini, R. Cummins, H. Xiao, M. Rottmayer, T. Reitz, Ink-jet printing of electrolyte and anode functional layer for solid oxide fuel cells, J. Power Sources 184 (2008) 191–196.
[12] M.A. Sukeshini, R. Cummins, T.L. Reitz, R.M. Miller, Ink-Jet Printing: A Versatile Method for Multilayer Solid Oxide Fuel Cells Fabrication, J. Am. Ceram. Soc. 92 (2009) 2913–2919.
[13] R.I. Tomov, M. Krauz, J. Jewulski, S.C. Hopkins, J.R. Kluczowski, D.M. Glowacka, B.A. Glowacki, Direct ceramic inkjet printing of yttria-stabilized zirconia electrolyte layers for anode-supported solid oxide fuel cells, J. Power Sources 195 (2010) 7160–7167.
[14] C. Li, H. Shi, R. Ran, C. Su, Z. Shao, Thermal inkjet printing of thin-film electrolytes and buffering layers for solid oxide fuel cells with improved performance, Int. J. Hydrogen Energy 38 (2013) 9310–9319.
[15] C. Wang, S.C. Hopkins, R.I. Tomov, R.V. Kumar, B.A. Glowacki, Optimisation of CGO suspensions for inkjet-printed SOFC electrolytes, J. Eur. Ceram. Soc. 32 (2012) 2317–2324.
[16] C. Wang, R.I. Tomov, R. Vasant Kumar, B.A. Glowacki, Inkjet printing of gadolinium-doped ceria electrolyte on NiO-YSZ substrates for solid oxide fuel cell applications, Journal of Materials Science 46 (2011) 6889–6896.
[17] N. Yashiro, T. Usui, K. Kikuta, Application of a thin intermediate cathode layer prepared by inkjet printing for SOFCs, J. Eur. Ceram. Soc. 30 (2010) 2093–2098.
[18] A.M. El-Toni, T. Yamaguchi, S. Shimizu, Y. Fujishiro, M. Awano, Development of a Dense Electrolyte Thin Film by the Ink-Jet Printing Technique for a Porous LSM Substrate, J. Am. Ceram. Soc. 91 (2007) 346–349.
[19] T.Y. Hill, T.L. Reitz, M.A. Rottmayer, H. Huang, Controlling Inkjet Fluid Kinematics to Achieve SOFC Cathode Micropatterns, ECS Journal of Solid State Science and Technology 4 (2015) P3015–P3019.
[20] G.D. Han, K.C. Neoh, K. Bae, H.J. Choi, S.W. Park, J.-W. Son, J.H. Shim, Fabrication of lanthanum strontium cobalt ferrite (LSCF) cathodes for high performance solid oxide fuel cells using a low price commercial inkjet printer, J. Power Sources 306 (2016) 503–509.
[21] N. Reis, C. Ainsley, B. Derby, Ink-jet delivery of particle suspensions by piezoelectric droplet ejectors, J. Appl. Phys 97 (2005) 094903.
[22] B. Derby, Inkjet printing ceramics: From drops to solid, J. Eur. Ceram. Soc. 31 (2011) 2543–2550.
[23] P.C. Duineveld, M.M. de kok, M. Buechel, A. Sempel, K.A.H. Mutsaers, P. van der Weijer, I.G.J. Camps, T. van den Biggelaar, J.-E.J.M. Rubingh, E.I. Haskal, Ink-Jet Printing of Polymer Light-Emitting Devices, in: Z.H. Kafafi (Ed.), Organic Light-Emitting Materials and Devices V, SPIE, 2002, pp. 59–67.
[24] R. Noguera, M. Lejeune, T. Chartier, 3D fine scale ceramic components formed by ink-jet prototyping process, J. Eur. Ceram. Soc. 25 (2005) 2055–2059.
[25] A.F. Routh, Drying of thin colloidal films, Rep. Prog. Phys 76 (2013) 046603.
[26] W.B. Russel, N. Wu, W. Man, Generalized Hertzian Model for the Deformation and Cracking of Colloidal Packings Saturated with Liquid, Langmuir 24 (2008) 1721–1730.
[27] A. Selçuk, A. Atkinson, Elastic properties of ceramic oxides used in solid oxide fuel cells (SOFC), J. Eur. Ceram. Soc. 17 (1997) 1523–1532.
[28] T. Ye, Z. Suo, A.G. Evans, Thin Film Cracking and the Roles of Substrate and Interface, International Journal of Solids Structures 29 (1992) 2639–2648.
[29] R.D. Deegan, O. Bakajin, T.F. Dupont, G. Huber, S.R. Nagel, T.A. Witten, Capillary flow as the cause of ring stains from dried liquid drops, Nature 389 (1997) 827–829.
[30] L. Kleiminger, T. Li, K. Li, G.H. Kelsall, Syngas (CO-H_2) production using high temperature micro-tubular solid oxide electrolysers, Electrochim. Acta 179 (2015) 565–577.
[31] L. Kleiminger, Solid Oxide Electrochemical Reactors and Proesses for Carbon Dioxide and Water Splitting, Ph.D Thesis, Imperial College London, UK, 2015.